Real–time haptic and visual simulation of bone dissection

Marco Agus   Andrea Giachetti   Enrico Gobbetti   Gianluigi Zanetti
Antonio Zorcolo

CRS4
VI Strada Ovest, Z. I. Macchiareddu, I-09010 Uta (CA), Italy
{magus,giach,gobbetti,zag,zarco}@crs4.it – http://www.crs4.it

Abstract

Bone dissection is an important component of many surgical procedures. In this paper, we discuss a haptic and visual implementation of a bone cutting burr, that it is being developed as a component of a training system for temporal bone surgery. We use a physically motivated model to describe the burr–bone interaction, that includes haptic forces evaluation, the bone erosion process and the resulting debris. The current implementation, directly operating on a voxel discretization of patient-specific 3D CT and MR imaging data, is efficient enough to provide real–time feedback on a low–end multi–processing PC platform.

1. Introduction

Bone dissection is an important component of many surgical procedures. In this paper, we discuss a real–time haptic and visual implementation of a bone cutting burr, that it is being developed as a component of a training simulator for temporal bone surgery. The specific target of the simulator is mastoidectomy, a very common operative procedure that consists in the removal, by burring, of the mastoid portion of the temporal bone. The system is designed to work on patient-specific volumetric object models directly derived from 3D CT and MRI images, and to provide realistic visual and haptic feedback, including secondary effects, such as the obscuring of the operational site due to the accumulation of bone dust and other burring debris. The need to provide real–time feedback to users, while simulating burring and related secondary effects, imposes stringent performance constraints. Our solution is based on a volumetric representation of the scene, and it harnesses the locality of the physical system evolution to model the system as a collection of loosely coupled components running in parallel on a multi-processor PC platform. This paper focuses on the modeling of bone burring. We refer the reader to[4] for details on the other system components.

In our model, the burr bit is represented as a region of space that samples the volumetric bone data to construct the elastic reaction and friction forces that the bone opposes to the burring. The sampling algorithm is similar in spirit to the Voxmap PointShell approach [11], even though here we use a volumetric region around the burr to select the bone voxels relevant to force calculation. Our algorithm for computing forces, loosely patterned on Hertz's contact theory [9], is robust and a smooth function of the burr position. The computed forces are transfered to the haptic device via a *sample–estimate–hold* [6] interface to stabilize the system. Bone erosion is modeled by postulating an energy balance between the mechanical work performed by the burr motor and the energy needed to cut the bone, that it is assumed to be proportional to the bone mass removed. The actual bone erosion is implemented by decreasing the density of the voxels that are in contact with the burr in a manner that is consistent with the predicted local mass flows. The process of accumulation of bone dust and other burring debris are then handled using simple, localized, sand-pile models.

The resulting bone dissection simulator provides haptic and visual renderings that are considered sufficient for training purposes.

The rest of the paper is structured as follows. Section two provides a brief description of the application area, while the following section is dedicated to the bone–burr interaction model. Section four describes how the latter model is integrated in the simulator system. Implementation details and results are reported in section five. Finally the last section reports on conclusions and future work.

2. Application area: mastoidectomy

Mastoidectomy is the most superficial and common surgery of the temporal bone. It consists of removal of the

air cavities just under the skin behind the ear itself, and it is performed for chronic infection of the mastoid air cells (mastoiditis). It is a surgical procedure undertaken by a wide range of surgeons in everyday practice. The mastoid air cells are widely variant in their anatomy and the main risks of the procedure are related to the detection and avoidance of the facial nerve, venous sinuses and "dura madre". Figure 1 shows a panoramic view of the mastoid region produced by the surgical simulator viewer.
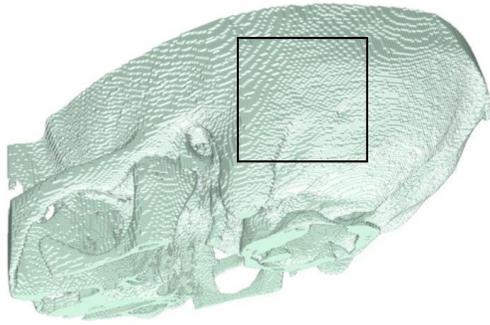
Figure 1. Surgical site. Mastoidectomy is performed in the region indicated by the rectangle. This 800x600 image has been produced in 70 ms by our simulator's volume renderer. The volumetric dataset is 256x256x128 and it is derived from CT images. CT data courtesy of dr. Emanuele Neri, Division of Diagnostic and Interventional Radiology, University of Pisa.

In the typical mastoidectomy surgical setup, see fig. 2, the surgeon looks at the region interested by the procedure via a stereoscopic microscope and holds in her hands a high speed burr and a sucker, that she uses, respectively, to cut the bone and to remove water (used to cool the burr bit) and bone paste produced by the mixing of bone dust with water, see fig. 3(a). Subjective analysis of video records, together with in-situ observations, [3], highlighted a correlation between burring behaviors and type and depth of bone. In the case of initial cortex burring, burr tip motions of around 0.8 cm together with sweeps over 2-4 cm were evident. Shorter (1–2 cm) motions with rapid lateral strokes characterized the post-cortex mastoidectomy. For deeper burring, 1 cm strokes down to 1mm were evident with more of a polishing motion quality, guided using the contours from prior burring procedures. The typical sweeping movement speed is of about 1 mm/s. Static burr handling was also noted, eroding bone tissue whilst maintaining minimal surface pressure.

The procedure requires bi-manual input, with high-quality force feedback for the dominant hand (controlling

(a) A real surgical setup   (b) A virtual surgical setup

Figure 2. Typical mastoidectomy surgical setup. The surgeon looks at the region interested by the procedure via a stereoscopic microscope and holds in his hands a high speed burr and a sucker. Photo (a) courtesy of Prof. Bob Stone, Virtual Presence Ltd.

the burr/irrigator), and only collision detection for the non-dominant one (controlling the sucker). Visual feedback requires a microscope-like device with at least 4 DOFs. The capability of replicating the effects caused by the intertwining of the different physical processes is of primary importance for training, see fig. 3 and [7, 3].

3. Bone–burr interaction model

A detailed mechanical description of a rotating burr cutting bone is complicated because it involves tracking the continuously changing free surface of the material being cut; the impact of the burr blades on the surface; the resulting stress distribution in the material; and the consequent plastic deformation and break–up.

To circumvent these complications, we have divided the cutting process in two successive steps. The first estimates the bone material deformation and the resulting elastic forces, given the relative position of the burr with respect to the bone. The second estimates the local rate of cutting of the bone by using a – postulated – energy balance between the mechanical work performed by the burr motor and the energy needed to cut the bone, that it is assumed to be proportional to the bone mass removed.

We will first describe this approach on a continuum model and then specialize the results to a discretized voxel grid.

(a) Mud formation
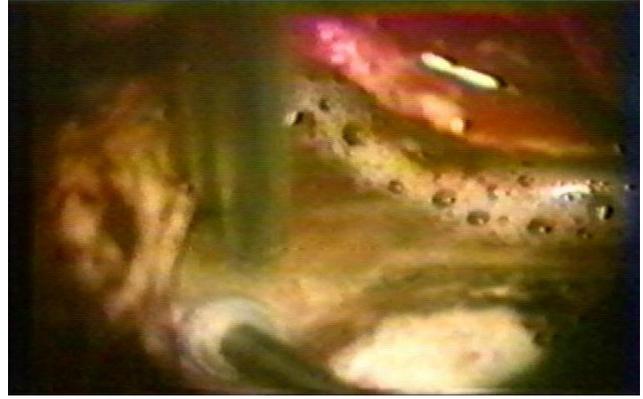
(b) Obscuring effects

Figure 3. Operation scene. These two images are typical examples of what is seen by the surgeon while performing mastoidectomy. In (a) it is clearly visible the paste created by the mixing of bone dust with water. If the paste and the water are not removed, they can obscure the field of view (b). Photos courtesy of Prof. Stefano Sellari Franceschini, ENT Surgery, Dept. of Neuroscience, University of Pisa.

3.1. Continuum description
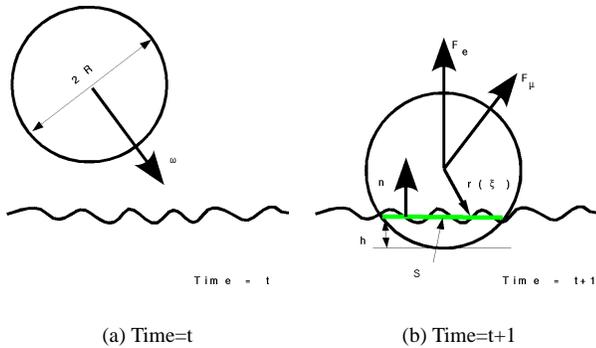
(a) Time=t   (b) Time=t+1

Figure 4. The impact of burr on bone. Here we represent two successive instants, at time t and $t+1$, of an idealized version of a surgeon burr. The burr has a spherical bit, of radius R, that is rotating with angular velocity $\vec{\omega}$. The surface S is the effective "contact surface" between the burr and the bone.

3.1.1 Forces evaluation

In figure 4 we represent two successive instants, at time t and $t+1$, of an idealized version of a surgeon burr. The burr

has a spherical bit, of radius R, that is rotating with angular velocity $\vec{\omega}$. At time step t the burr is just outside the bone material, while at the next time step it is intersecting the bone surface. In the following, we will refer to the sphere representing the burr bit as B, and to the "contact surface" between the burr and the bone as S.

All the relevant geometrical information is contained in the volumetric distribution of the bone material. We use a characteristic function $\chi(\vec{r})$ to indicate the presence/absence of bone, where $\vec{r}$ is measured from the center of B. The first two moments of χ, restricted to the region contained in B are, respectively,

$$M \quad = \quad \int_{r<R} dr^3 \chi(\vec{r}), \qquad (1)$$

$$\vec{M_1} \quad = \quad \int_{r<R} dr^3 \chi(\vec{r})\vec{r}. \qquad (2)$$

We can now estimate the normal direction, $\hat{\mathbf{n}}$, to S, as $\hat{\mathbf{n}} = -\vec{M_1}/|M_1|$ and the "thickness" h of B immersed in the bone, by solving $M = \pi h^2(R - \frac{h}{3})$. We can now derive, assuming that $\frac{h}{R} << 1$, and using Hertz's contact theory [9], an expression for the total force, $\vec{F_e}$, exerted on the burr by the elastic deformation of the bone:

$$\vec{F_e} = C_1 R^2 (\frac{h}{R})^{\frac{3}{2}} \hat{\mathbf{n}}, \qquad (3)$$

where C_1 is a dimensional constant, that describes the elastic properties of the material. Moreover, we can give an

expression for the pressure, $\vec{P}(\vec{\xi})$, exerted by the burr on the point $\vec{\xi}$ of S:

$$\vec{P}(\vec{\xi}) = -\frac{3}{2\pi a^2}\sqrt{1 - \frac{|\vec{\xi}|^2}{a^2}}\vec{F}_e, \tag{4}$$

where $\vec{\xi}$ is measured from the center of S, see fig. 4(b), and a is the radius of the contact region. In Hertz's contact theory, a can be estimated as

$$a = (C_1 R)^{\frac{1}{3}} F_e^{\frac{1}{3}}. \tag{5}$$

From equation 4, we can estimate the frictional force, $\vec{F}_\mu$, that the bone will oppose to the burr rotation:

$$\vec{F}_\mu = \mu \int_{\xi < a} d\sigma P(\vec{\xi}) \frac{\vec{r}(\vec{\xi}) \times \vec{\omega}}{|\vec{r}(\vec{\xi})||\vec{\omega}|}, \tag{6}$$

where μ is a friction coefficient, that links the frictional forces for unit area to the locally exerted pressure.

The total force that should be returned by the haptic feedback device is, therefore, $\vec{F}_T = \vec{F}_e + \vec{F}_\mu$.

3.1.2 Erosion modeling

We model the cutting of the burr by assuming that all the power spent by working against the frictional forces on a "contact surface" element $d\sigma$ goes toward the erosion of the bone material in contact with the surface. In other words, we equate

$$\mu P(\vec{\xi})\omega r(\vec{\xi})\left(1 - (\frac{\vec{r}(\vec{\xi}) \cdot \vec{\omega}}{|\vec{r}(\vec{\xi})||\vec{\omega}|})^2\right)d\sigma = \alpha\phi(\vec{\xi})d\sigma, \tag{7}$$

where α is a dimensional constant and $\phi(\vec{\xi})$ is the mass flux at the contact surface point $\vec{\xi}$. Using the mass flux ϕ one can update the position of the bone surface.

The formulas above have been written with the implicit assumption that the burr blades are very small with respect to the burr bit radius, and that their effect can be absorbed in the friction constant μ and in the "erosion constant" α. Even though this is, in general, false, and Hertz's theory is, strictly speaking, only valid for small elastic deformations, this formulation provides a computationally tractable, robust, expression for the response forces that, at least in the limit of small h, is physically reasonable.

3.2. Discretized description

3.2.1 Forces evaluation

In the simulator, the bone distribution is only known at the level of a volumetric grid discretized in cubic voxels. Eqs. (1,2,6) need, therefore, to be translated and re–interpreted.

A direct translation will transform integrals in sums over the voxels that have non null intersection with B. The evaluation of each voxel contribution is computationally complex, since it requires to find the intersections between B and the cube defining the voxel. To simplify matters, we are approximating the voxels with spheres of the same volume, centered at the voxel center, $\vec{c}_i$, whit the origin at the center of B. The radius of the voxel spheres, η, is, therefore, defined by $\frac{4}{3}\pi\eta^3 = \ell^3$, where ℓ is the length of the voxel side.

Using this approximation, it is trivial to derive simple formulas that express, in terms of the distance $d = |\vec{c}_i|$, the volume, ΔV, of the intersection region; the area, $\Delta\sigma$, of the "intersection surface" and the actual distance, r, from the center of the intersection surface to the center of B.

$$\Delta v(d) = \frac{\pi}{12}(d^3 - 6(R^2 + \eta^2)d + 8(R^3 + \eta^3) \tag{8}$$

$$- 3(\eta^2 - R^2)^2\frac{1}{d}) \tag{9}$$

$$\Delta\sigma(d) = \frac{\pi}{4}(2(\eta^2 + R^2) - d^2 - (\eta^2 - R^2)^2\frac{1}{d^2}) \tag{10}$$

$$r(d) = \frac{1}{2}d + \frac{R^2 - \eta^2}{2}\frac{1}{d} \tag{11}$$

The required integrals then become

$$M^* = \sum_i \Delta V(|\vec{c}_i|)\chi_i \tag{12}$$

and

$$\vec{M}_1^* = \sum_i \Delta V(|\vec{c}_i|)\chi_i\frac{r_i}{d_i}\vec{c}_1. \tag{13}$$

To estimate the friction force, $\vec{F}_\mu$ we convert the area integral (6) in

$$\vec{F}_\mu = \mu\sum_i \Delta\sigma(|\vec{c}_i|)P(\vec{\xi}_i)\frac{\vec{c}_i \times \vec{\omega}}{|\vec{c}_i||\vec{\omega}|}, \text{ with } \vec{\xi}_i = \frac{r_i}{d_i}(\vec{c}_i - \frac{(\vec{\omega} \cdot \vec{c}_i)}{\omega^2}\vec{\omega}). \tag{14}$$

The power spent by the frictional forces on a voxel is then

$$\mu P(\xi_i)\omega r_i(\vec{\xi}_i)\left(1 - (\frac{\vec{c}_i \cdot \vec{\omega}}{|\vec{c}_i||\vec{\omega}|})^2\right)\Delta\sigma_i = \alpha\phi_i\Delta\sigma_i, \tag{15}$$

where ϕ_i is the mass flux per unit surface coming out of voxel i, via surface $\Delta\sigma_i$. To evaluate P we use formula (4), where for a we use the "effective" radius of the contact surface $a^* = \sqrt{2Rh - h^2}$.

3.2.2 Erosion modeling

Using the fluxes ϕ_i we can now erode the voxels in the intersection region. In our current implementation, we associate a 8 bit counter with each voxel, representing the voxel density, and decrease it by a value proportional to the "assumed" amount of removed mass, $\Delta M_i = \Delta t\Delta\sigma\phi_i$, where

Δt is the time step of the simulation, and the mass, M_i, contained in the voxel i. The bone material in the temporal bone area has a morphological structure that ranges from compact bone, e.g., close to the outer skull surface, to a porous, "trabecular", consistency. The porous scale ranges from few millimeters down to scales well beyond the resolution of the medical imaging devices. In our model, the subscale modeling of the trabecular structures is absorbed in a voxel dependent erosion constant α.

As it was mentioned before, the burring of the bone produces dust that mixes with water in a paste, "mud", clearly visible in figure 3(a). The paste material has a quite complex behavior, from sand–like to gel–like. The water paste mixture needs to be continuously removed, otherwise it can obscure the field of view as it is seen in figure 3(b). Although the presence of the water/paste mixture is essentially irrelevant with respect to the interaction between the burr and the bone, its presence cannot be neglected in the creation of the visual feed–back, since its "obscuring" effects constitute the principal cue to the user for the use of the sucker device.

A direct, "physically correct", simulation of the dust-water system would require, to be able to capture all the dynamically relevant length scales, a very fine spatial resolution and it would be computationally incompatible with the real–time requirements of the simulation. Therefore, we are modeling the dust/fluid dynamics using what essentially amounts to an hybrid particles/sand pile model [12, 10]. The dust/fluid system is fed by the burring but its dynamics does not influence the haptic force evaluation.

Figure 8 shows the beginning of a typical bone cutting sequence performed in the mastoid region.

3.3. Sample–Estimate-Hold Interface

A direct transmission of the computed forces to the haptic device is, in the case of "almost rigid" contacts, usually plagued by mechanical instabilities. The typical solution for this problem is the introduction of an artificial, "virtual", coupling between the haptic device and the virtual environment [5, 1].

In our system, we use a *sample–estimate–hold* approach [6] to remove the excess energy injected by the standard zero–order hold of force employed by the haptic device drivers. With this technique, we compute the force that is sent to the haptic device based on the previous zero–order representations produced at regular intervals by our burr–bone interaction model. This new value of force, when held over the corresponding sampling interval, approximates the force–time integral more closely than the usual zero–order hold [6].

4. System integration

Our technique for bone dissection simulation has been integrated in a prototype training system for mastoidectomy. We have exploited the difference in complexity and frequency requirements of the visual and haptic simulations by modeling the system as a collection of loosely coupled concurrent components. Logically, the system is divided in a "fast" subsystem, responsible for the high frequency tasks (surgical instrument tracking, force feedback computation, bone erosion), and a "slow" one, essentially dedicated to the production of data for visual feedback. The "slow" subsystem is responsible for the global evolution of the water, bone dust and bone paste. The algorithms used to control the simulations are local in character and they are structured so that they communicate only via changes in the relevant, local, substance densities. This arrangement leads naturally to a further break-up of the slow subsystem in components, each dedicated to the generation of a specific visual effect, and thus to a parallel implementation on a multiprocessor architecture. The system runs on two interconnected multiprocessor machines. The data is initially replicated on the two machines. The first is dedicated to the high-frequency tasks: haptic device handling and bone removal simulation, which run at 1 KHz. The second concurrently runs, at about 15–20 Hz, the low-frequency tasks: bone removal, fluid evolution and visual feedback. Since the low-frequency tasks do not influence high-frequency ones, the two machines are synchronized using one-way message passing, with a dead reckoning protocol to reduce communication bandwidth. A specialized volumetric rendering component, exploiting multi–texturing and register combiner OpenGL extensions [8], provides the required high frequency visual feedback.

5. Implementation and results

Our current configuration is the following:

- a single-processor PII/600 MHz with 256 MB PC133 RAM for the high-frequency tasks; two threads run in parallel: one for the haptic loop (1KHz), and one for sending volume and instruments position updates to the other machine;

- a dual-processor PIII/600 MHz with 512 MB PC800 RAM and a NVIDIA GeForce 2 GTS and running a 2.4 linux kernel, for the low frequency tasks; three threads are continuously running on this machine: one to receive volume and position updates, one to simulate bone removal and fluid evolution, and one for visual rendering;

(a) F_e (b) F_μ
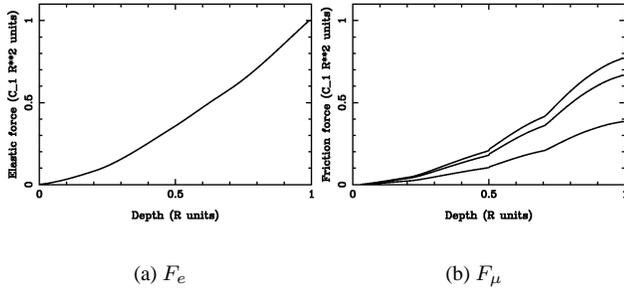
Figure 5. Virtual bone reaction against burr penetration. The computations are done in absence of erosion, $\alpha = \infty$, using the actual force evaluation kernel of the force–feedback loop. In (a) we show the "elastic" response of the material, measured in units of $C_1 R^2$, as a function of the burr tip penetration depth in units of the burr bit radius R. Fig. (b) illustrates the "frictional" response of the material, with $\mu = 1/2$ and for different angles $\theta, \theta = 30°, 60°, 90°$, between the surface normal and $\hat{\omega}$. The strength of F_μ increases for increasing $\sin(\theta)$. The knees in the F_μ curves correspond to the intersection of the burr bit with a deeper bone voxel layer.

- a Phantom Desktop haptic device for the dominant hand; the device is connected to the single processor PC. It provides 6DOF tracking and 3DOF force feedback for the burr/irrigator;

- a Phantom 1.0 haptic device for the non-dominant hand; the device is connected to the single processor PC. It provides 6DOF tracking and 3DOF force feedback for the sucker;

- an n-vision VB30 binocular display for presenting images to the user; the binoculars are connected to the S-VGA output of the dual processor PC.

The performance of the prototype is sufficient to meet timing constraints for display and force-feedback, even though the computational and visualization platform is made only of affordable and widely accessible components. We are currently using a volume of 256x256x128 cubical voxels (0.3 mm side) to represent the region where the operation takes place. The force–feedback loop is running at 1 KHz using a 5x5x5 grid around the tip of the instruments for force computations. The computation needed for force evaluation and bone erosion takes typically $20\mu s$, and less than $200\mu s$ in the worst case configuration.

(a) F_e (b) F_μ
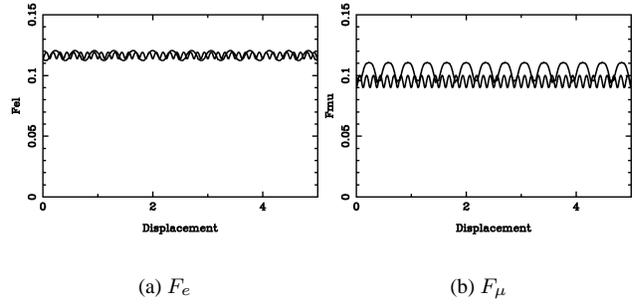
Figure 6. Sliding motion, constrained experiment. The reaction of the flat surface of virtual bone to the sliding motion of a burr bit immersed at a depth of $R/4$. Fig. (a,b) show, respectively, the "elastic" and the "frictional" force response of the material, measured in units of $C_1 R^2$, as a function of the distance traveled along the plane measured in R units. The pair of curves in each figure correspond to a sliding motion over a bone surface aligned along, respectively, one of the voxel discretization axis, and a plane with normal $[0, \frac{1}{\sqrt{2}}, \frac{1}{\sqrt{2}}]$. The fluctuations in the force values are due to the "voxel sphere" approximation used to compute F. The difference in the wavelength of the fluctuations is a factor of $\sqrt{2}$ as expected.

In the following we will report on a series of experiments done using the prototype described above.

5.1. Force Evaluation

Figure 5 shows the reaction of the virtual bone against burr penetration. The computations are done in absence of erosion, $\alpha = \infty$, and using the actual force evaluation kernel of the force–feedback loop.

Figure 5(a) illustrates the "elastic" response of the material, measured in units of $C_1 R^2$, as a function of the burr tip penetration depth measured in units of the burr bit radius R. Figure 5(b) illustrates the "frictional" response of the material, with $\mu = 1/2$ and for different angles $\theta, \theta = 30°, 60°, 90°$, between the surface normal and $\hat{\omega}$. The strength of F_μ increases for increasing $\sin(\theta)$. The knees in the F_μ curves correspond to the intersection of the burr bit with a deeper bone voxel layer.

Figure 6 shows the reaction of the virtual bone, again in runs with $\alpha = \infty$, to a sliding motion of the burr bit, immersed at a depth of $R/4$, over a flat bone surface. Fig. 6(a,b) show, respectively, the "elastic" and the "fric-
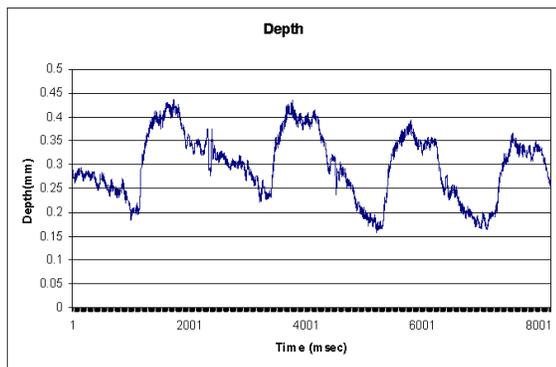
(a) Depth
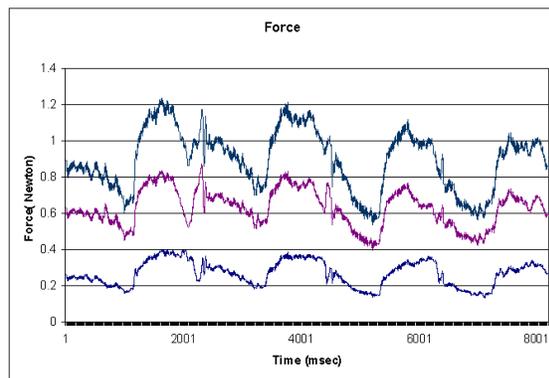
(b) Forces

Figure 7. Bone erosion, polishing movement. A "free–hand" experiment where bone is eroded by a polishing movement. The sliding speed is about 10mm/sec, and $\alpha = 3.1 \times 10^6$mm^2/sec^2. Fig. (a) shows the depth of the burr below the surface level as a function of time. Fig. (b) reports the components of the force contributions and the total force applied to the haptic display during the movement. The lower line is the friction force $\vec{F}_\mu$, the middle line is the elastic force $\vec{F}_{el}$, and the upper line is the total force $\vec{F}_{tot}$.

tional" force response of the material, measured in units of $C_1 R^2$, as a function of the distance traveled along the plane measured in R units. The pair of curves in each figure correspond to a sliding motion over a bone surface aligned along, respectively, one of the voxel discretization axis, and a plane with normal $[0, \frac{1}{\sqrt{2}}, \frac{1}{\sqrt{2}}]$. The fluctuations in the force values are due to the "voxel sphere" approximation used to compute F. The difference in the wavelength of the fluctuations is a factor of $\sqrt{2}$ as expected.

5.2. Bone erosion

Figure 7 illustrates a "free–hand" experiment where bone is eroded by a polishing movement. The movement is similar to the one described in the previous subsection, with a sliding speed of about 10mm/sec, and $\alpha = 3.1 \times 10^6$mm^2/sec^2. Figure 7(a) shows the depth of the burr below the surface level as a function of time, while fig. 7(b) reports the components of the force contributions and the total force applied to the haptic display during the movement.

We have gathered initial feedback about the prototype system from specialist surgeons from the University of Pisa that are collaborating to this research. Subjective input is being used to tune the parameters that control force feedback. The overall realism of the simulation is considered

sufficient for training purposes. Fig. 8 shows a typical erosion sequence. A demonstration movie is available on the IERAPSI project web site [2].

6. Conclusions and Future Work

We have presented a haptic and visual implementation of a bone cutting burr, that it is being developed as a component of a training system for temporal bone surgery. We use a physically motivated model to describe the burr–bone interaction, that includes haptic forces evaluation, the bone erosion process and the resulting debris. The current implementation, directly operating on a voxel discretization of patient-specific 3D CT and MR imaging data, is efficient enough to provide real–time feedback on a low–end multi–processing PC platform.

While subjective input from selected end users is encouraging, it would be of extreme interest to compare our results with direct forces measurements obtained by drilling actual samples. Since, to our knowledge, there are no available data on the subject in literature, we are currently defining an experimental setup and measurement procedures.

In our simulator, we are currently using datasets that have the same resolution of the original medical imaging data, and we are not differentiating between compact and trabecular bone. It is our intention to explore the possibil-

(a)   (b)   (c)
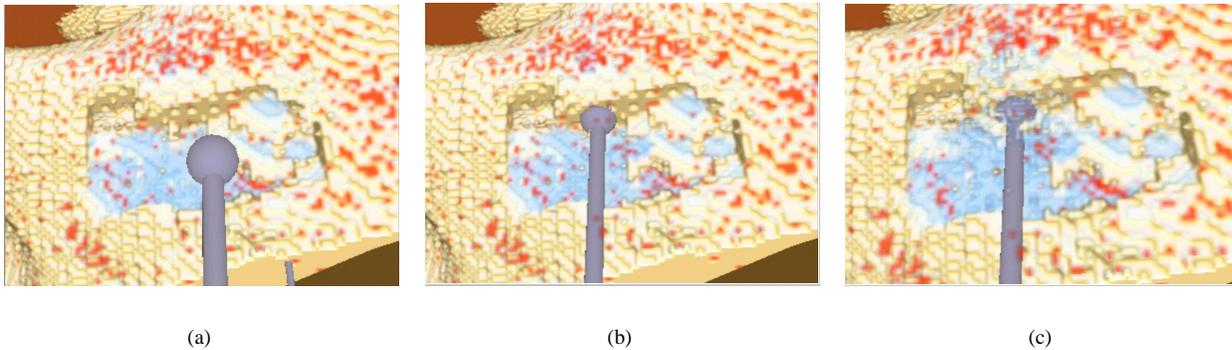
Figure 8. A virtual burring sequence. Here we show a typical bone cutting sequence performed in the mastoid region. The accumulation of debris, and its masking effects, is clearly visible.

ity of running the simulator on synthetically refined datasets obtained by using sub–voxel trabecular bone modeling.

7. Acknowledgments

References

[1] R. Adams and B. Hannaford. Stable haptic interaction with virtual environments. *IEEE Transactions on Robotics and Automation*, 15(3):465–474, 1999.

[2] M. Agus, F. Bettio, A. Giachetti, E. Gobbetti, G. Zanetti, and A. Zorcolo. Real–time haptic and visual simulation of bone dissection. Video demonstration, http://www.crs4.it/ierapsi, 2001.

[3] M. Agus, A. Giachetti, E. Gobbetti, G. Zanetti, N. W. John, and R. J. Stone. Mastoidectomy simulation with combined visual and haptic feedback. In J. D. Westwood, H. M. Hoffmann, G. T. Mogel, and D. Stredney, editors, *Medicine Meets Virtual Reality 2002*, Amsterdam, The Netherlands, Jan. 2002. IOS Press.

[4] M. Agus, A. Giachetti, E. Gobbetti, G. Zanetti, and A. Zorcolo. A multiprocessor decoupled system for the simulation of temporal bone surgery. Technical report, IERAPSI (IST-1999-12175), 2001. Submitted for publication.

[5] J. Colgate. Issues in the haptic display of tool use. In *Proceedings of ASME Haptic Interfaces for Virtual Environment and Teleoperator Systems*, pages 140–144, 1994.

[6] R. Ellis, N. Sarkar, and M. Jenkins. Nomerical methods for the force reflection of contact. *ASME Transactions on Dynamic Systems, Modeling, and Control*, 119(4):768–774, 1997.

[7] N. W. John, N. Thacker, M. Pokric, A. Jackson, G. Zanetti, E. Gobbetti, A. Giachetti, R. J. Stone, J. Campos, A. Emmen, A. Schwerdtner, E. Neri, S. S. Franceschini, and F. Rubio. An integrated simulator for surgery of the petrous bone. In J. D. Westwood, editor, *Medicine Meets Virtual Reality 2001*, pages 218–224, Amsterdam, The Netherlands, January 2001. IOS Press.

[8] M. J. Kilgard, editor. *NVIDIA OpenGL Extension Specifications*. NVIDIA Corporation, May 2001.

[9] L. Landau and E. Lifshitz. *Theory of elasticity*. Pergamon Press, 1986.

[10] X. Li and J. Moshell. Modeling soil: Realtime dynamic models for soil slippage and manipulation. In *Computer Graphics Proceedings, Annual Conference Series*, pages 361–368, 1993.

[11] W. A. McNeely, K. D. Puterbaugh, and J. J. Troy. Six degrees-of-freedom haptic rendering using voxel sampling. In A. Rockwood, editor, *Siggraph 1999*, Annual Conference Series, pages 401–408, Los Angeles, 1999. ACM Siggraph, Addison Wesley Longman.

[12] J. H. R.W. Sumner, J.F. O'Brien. Animating sand, mud and snow. *Computer Graphics Forum*, 18:1, 1999.